

Ethylene Dehydrogenation on Pt_{4,7,8} Clusters on Al₂O₃: Strong Cluster Size Dependence Linked to Preferred Catalyst Morphologies

Eric T. Baxter,^{†,‡} Mai-Anh Ha,^{‡,§} Ashley C. Cass,[†] Anastassia N. Alexandrova,^{*,‡,§,ID} and Scott L. Anderson^{*,†,ID}

[†]Department of Chemistry, University of Utah, Salt Lake City, Utah 84112, United States

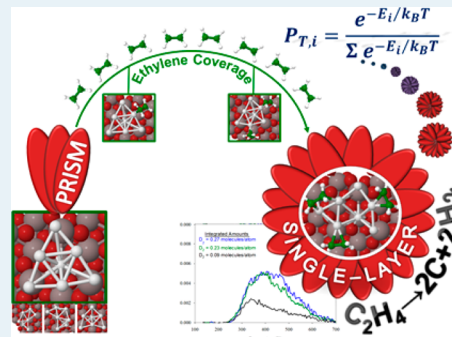
[‡]Department of Chemistry and Biochemistry, University of California, Los Angeles, California 90095, United States

[§]California NanoSystems Institute, Los Angeles, California 90095, United States

Supporting Information

ABSTRACT: Catalytic dehydrogenation of ethylene on size-selected Pt_n ($n = 4, 7, 8$) clusters deposited on the surface of Al₂O₃ was studied experimentally and theoretically. Clusters were mass-selected, deposited on the alumina support, and probed by a combination of low energy ion scattering, temperature-programmed desorption and reaction of C₂D₄ and D₂, X-ray photoelectron spectroscopy, density functional theory, and statistical mechanical theory. Pt₇ is identified as the most catalytically active cluster, while Pt₄ and Pt₈ exhibit comparable activities. The higher activity can be related to the cluster structure and particularly to the distribution of cluster morphologies accessible at the temperatures and coverage with ethylene in catalytic conditions. Specifically, while Pt₇ and Pt₈ on alumina have very similar prismatic global minimum geometries, Pt₇ at higher temperatures also has access to single-layer isomers, which become more and more predominant in the cluster catalyst ensemble upon increasing ethylene coverage. Single-layer isomers feature greater charge transfer from the support and more binding sites that activate ethylene for dehydrogenation rather than hydrogenation or desorption. Size-dependent susceptibility to coking and deactivation was also investigated. Our results show that size-dependent catalytic activity of clusters is not a simple property of single cluster geometry but the average over a statistical ensemble at relevant conditions.

KEYWORDS: cluster catalysis, cluster fluxionality, dehydrogenation, selectivity, theory, experiment



INTRODUCTION

The subnano clusters are known to have special catalytic reactivity.^{1–4} For example, a specific range of cluster size often results in preferential reaction pathways or significantly altered reactivity because in the subnano regime clusters are affected by size-dependent electronic and geometric structure. One issue complicating this situation is that there may be multiple thermally accessible cluster structures with significantly different electronic and binding site properties. Here, we use a combination of experimental probes of cluster structure and binding site distributions together with density functional theory (DFT) to explore the range of thermally accessible structures and study the effects of size-dependent cluster structure on ethylene binding and dehydrogenation.

Platinum's ability to (de)hydrogenate hydrocarbons is well-documented, and it is of interest to see if small clusters of Pt can be good dehydrogenation catalysts with useful selectivity that might enable more economical use of precious metals in catalysis. An important part of the problem is the stability of small clusters with respect to both sintering or agglomeration and deactivation by carbon deposition (coking).^{5–8}

This work focuses on catalytic dehydrogenation on Pt₄, Pt₇, and Pt₈ clusters supported on alumina. Significant differences

have been found experimentally between Pt₇ and Pt₈, here and elsewhere, and much of our effort is focused on understanding why. Pt₄ was included as an example of a smaller cluster. In this size range, strong size effects on activity have been noted. Vajda et al. observed Pt_{8–10}'s activity of 40–100 times for oxidative dehydrogenation of propane;² Roberts et al. observed strongly size-dependent activity for CO oxidation, which was correlated to changes in both the valence electronic structure and the number of CO binding sites on top of the clusters.⁹

There is evidence suggesting that such effects may be at least partly related to a structural transition occurring around Pt₇ and Pt₈. Low energy ion scattering (ISS) for Pt_n/alumina/Re(0001) showed an abrupt ~15% drop in the Pt ISS signal going from Pt₇ to Pt₈, indicating a transition to morphologies where fewer Pt atoms are in the ISS-accessible top layer of the clusters.⁹ As discussed below, we verified that the effect also occurs for the Pt_n/alumina/Ta(110) system studied here. Indeed, the drop between Pt₇ and Pt₈ is actually somewhat larger (~24%) for alumina/Ta(110). The inference of a drop in the fraction of Pt

Received: February 7, 2017

Revised: March 23, 2017

Published: March 28, 2017

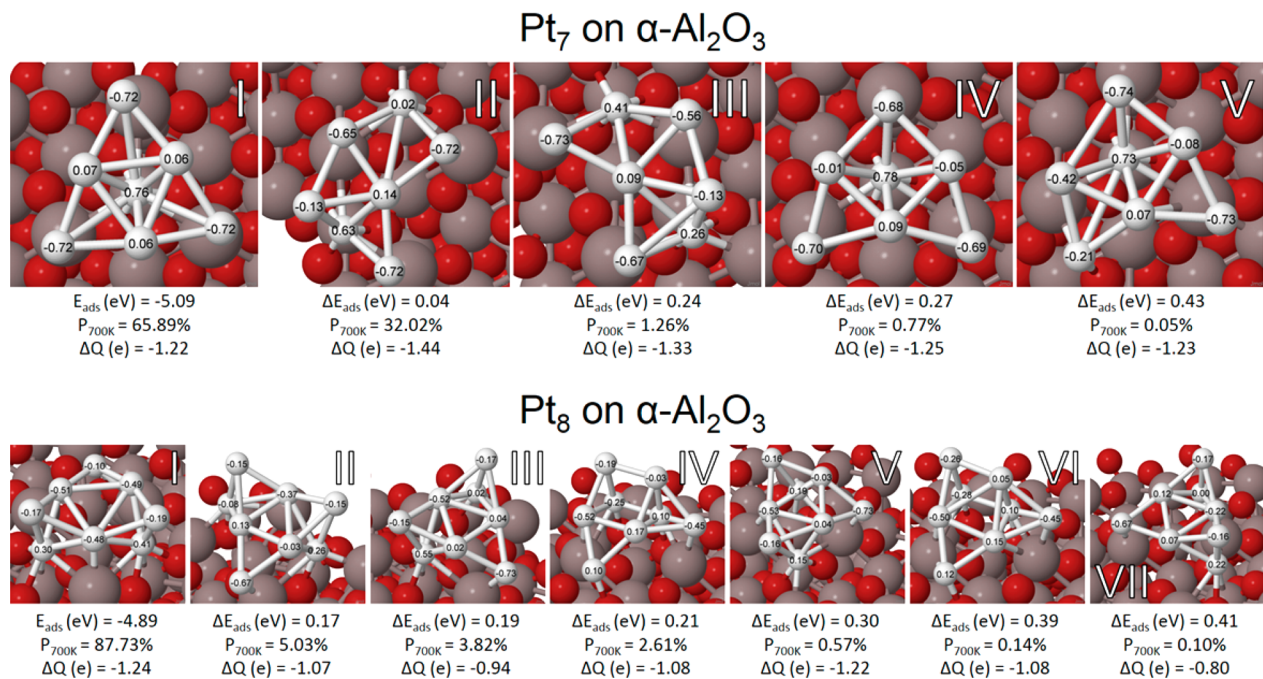


Figure 1. Lowest-energy minima of adsorbed Pt₇ and Pt₈ with adsorption energies (E_{ads}), Boltzmann population at catalytic temperature of 700 K ($P_{700\text{K}}$), and charge transfer from the support to the cluster (ΔQ).

in the surface layer at Pt₈ is consistent with a scanning tunneling microscopy study of Pt_n/TiO₂ by Watanabe et al.,^{10,11} who observed a transition from single- to multilayer clusters between Pt₇ and Pt₈. Such transitions change the number and type of adsorbate binding sites exposed on the clusters; however, it is important to recognize that adsorbate binding can drive cluster isomerization, i.e., it is necessary to characterize both adsorbate-free and adsorbate-covered structures. As shown below, Pt₇ is able to adsorb more ethylene than Pt₄ or Pt₈, on either a per Pt atom or per cluster basis, consistent with additional Pt atoms exposed in the surface layer. DFT allows this effect and the earlier ISS observations to be explained.

RESULTS AND DISCUSSION

We begin by discussing DFT results for adsorbate-free Pt₇ and Pt₈ on α -alumina, as summarized in Figure 1 and Table S4. The charges on the Pt atoms in each structure are indicated and discussed below.

Cluster Catalyst Structures. Small Pt clusters have many structural isomers with similar energies,¹² and both Pt₇/alumina and Pt₈/alumina are found to have 5–7 isomers of very different geometries, predicted to be populated in the 450–700 K temperature range where dehydrogenation is observed. At the elevated temperatures relevant to catalysis and in the limit of no kinetic trapping, strong structural fluxionality and the presence of several isomers are expected.¹³ Because catalytic properties may be dominated by any one or few of the isomers, it is important to consider all thermally relevant structures.¹⁴ We will generally describe the structures as being either single-layer, where all Pt atoms are exposed in the surface layer, or prismatic, where one or more atoms are buried under the cluster surface. The lowest energy isomers of Pt₇ and Pt₈ on alumina are shown in Figure 1 together with their Bader charges and Boltzmann populations at 700 K. Pt₇ is found to have both single layer and prismatic structures in the thermally

accessible set, with prismatic geometries (global minimum and fourth isomer) comprising 66.7% of the Boltzmann population at 700 K and with the balance being single-layer geometries (second, third, and fifth isomers). In contrast, all of the accessible isomers of Pt₈ are prismatic.

The calculated structures provide an explanation for the ISS observation that the fraction of Pt in surface layer drops between Pt₇ and Pt₈.⁹ ISS was done at 130 K; thus, if the isomer distribution is equilibrated, only the lowest energy structures of each cluster would have significant populations. For Pt₇, this structure is prismatic but exposes 6 of its 7 atoms (i.e., ~86%) in the ISS-accessible surface layer. The lowest energy isomer of Pt₈ exposes only 6 of its 8 atoms (75%) in the surface layer; thus, we would predict a ~12.5% drop in ISS intensity between Pt₇ and Pt₈. It is not unlikely; however, that there are barriers to isomerization, such that some higher energy structures remain as the sample is cooled. To the extent that this kinetic trapping occurs, it would tend to give an even larger intensity drop between Pt₇ and Pt₈ because Pt₇ has several single layer isomers where 100% of the Pt would be detectable, whereas all of the Pt₈ isomers are prismatic.

At higher temperatures, relevant to the temperature-programmed desorption and reaction (TPD/R) experiments, the diversity of geometries of Pt₇ offers a richer set of binding sites for ethylene as opposed to the more uniform structures populated for Pt₈, and this should be reflected in the chemical activity.

Size-Dependent Catalytic Activity. The chemical properties of the clusters, as probed by TPD/R, are summarized in Figure 2 for two consecutive TPD/R experiments on samples containing Pt₄, Pt₇, and Pt₈. For each experiment, the samples were dosed with 5 L of C₂D₄ at 150 K and then cooled to ~130 K prior to each TPD/R heat ramp (3 K/sec). The figure shows results for the two species, C₂D₄ and D₂, observed to have significant desorption signals. Desorption is reported in terms of C₂D₄ or D₂ molecules desorbing per Pt atom per second,

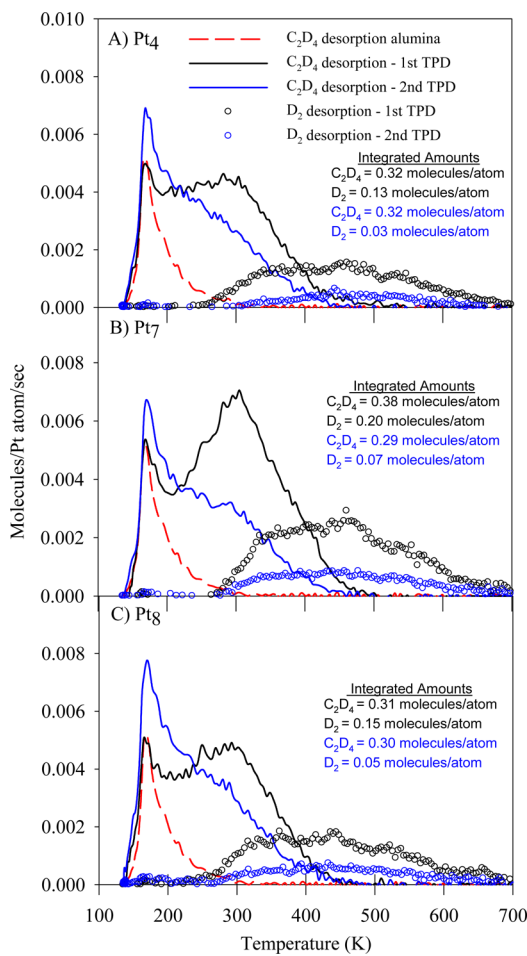


Figure 2. Desorption of unreacted C₂D₄ (solid) and D₂ products (circles) during the 1st and 2nd consecutive TPR runs. Each TPR measurement was made after a 5 L C₂D₄ exposure to Pt_n/alumina ($n = 4, 7$, or 8) at 150 K. The dashed red line shows desorption of unreacted C₂D₄ from the cluster-free alumina support and is scaled as if the sample contained an identical Pt loading as the Pt_n/alumina samples. Each set of spectra results from individual experiments. Included in each frame is the total integrated desorption of C₂D₄ and D₂ per Pt atom for each experiment.

taking advantage of the fact that we know the Pt loading quite precisely ($1.5 \times 10^{14}/\text{cm}^2$). The D₂ signals were corrected for the contribution from mass spectrometer cracking of desorbing C₂D₄, and the uncorrected data are reported in Figure S1. To avoid interference from high background signals at masses 2 and 28, most experiments were done with C₂D₄. Experiments with C₂H₄ were also done to look for acetylene desorption; however, none was observed. In addition, no signal for ethane was observed, indicating that hydrogenation is negligible under these conditions.

C₂D₄ desorption from the cluster-free alumina/Ta(110) support is shown for comparison to the Pt_n/alumina results. Only the result of the first TPD/R run is shown because the second run was identical. To allow direct comparison, the data for cluster-free alumina were scaled as if these samples also contained the same amount of Pt as the Pt_n/alumina samples. For the cluster-free alumina film, C₂D₄ began to desorb at the TPD starting temperature with desorption peaking at ~165 K and rapidly declining at higher temperatures. After correcting for the contribution from C₂D₄ cracking in the mass spectrometer, the D₂ signal is zero, i.e., all ethylene adsorbed

on the alumina film desorbs intact. The integrated number of C₂D₄ molecules desorbing from alumina is $\sim 7 \times 10^{12}/\text{cm}^2$, i.e., on the order of 0.01 ML. The low intensity indicates that ethylene does not bind stably to most sites on the alumina film at 150 K but that there are a few stable binding sites, presumably corresponding to defects in the alumina surface. Even these defect sites bind C₂D₄ weakly such that it desorbs intact, well below room temperature.

For the cluster-containing samples, ethylene desorption also begins as the heat ramp is started with a sharp peak near ~165 K for all three cluster sizes. There is weak D₂⁺ signal at low temperatures (Figure S1), but this is entirely due to dissociative ionization of desorbing C₂D₄. Both the temperature dependence and intensity of the 165 K peak match those for cluster-free alumina, indicating that this low temperature feature is simply due to C₂D₄ desorbing from defect sites on the alumina film. The fact that this low temperature component is not significantly affected by deposition of 0.1 ML equivalent of Pt_n suggests that the clusters do not diffuse to and occupy these defect sites, at least in the <300 K range where Pt_n deposition, C₂D₄ exposure, and desorption of the low temperature feature occur.

For Pt_n-containing samples, there is also a broad C₂D₄ desorption component extending between ~200 and 420 K, which clearly results from ethylene bound to the Pt clusters. The peak temperature of this component is ~280 K for Pt₄ and Pt₈ and ~300 K for Pt₇, and the intensity is also significantly higher for the Pt₇-containing sample. Below ~250 K (Pt₄, Pt₈) or ~275 K (Pt₇), only intact C₂D₄ desorption is observed, but at higher temperatures, D₂ desorbs in a broad component extending to 650 K. In each case, the onset of D₂ desorption is just below the peak C₂D₄ desorption temperature, as would be expected if dehydrogenation to generate D₂ is in competition with C₂D₄ desorption.

The figure also lists the integrated amounts of C₂D₄ and D₂ observed to desorb from each sample, given in terms of number of molecules desorbing per Pt atom. Desorption/cm² can be obtained simply by multiplying by the Pt coverage (1.5×10^{14} Pt atoms/cm²). These numbers include desorption from both alumina and Pt_n sites, and to compare the Pt_n-only desorption, it is necessary to subtract the alumina contribution, equivalent to ~0.08 C₂D₄/Pt atom. Thus, in the first TPD/R experiment, the corrected desorption is 0.24 C₂D₄ and 0.13 D₂ molecules per Pt atom for Pt₄, compared to 0.30 C₂D₄ and 0.20 D₂ for Pt₇, and 0.23 C₂D₄ and 0.15 D₂ for Pt₈.

No additional D₂ desorption was observed in select experiments where the temperature was ramped to 900 K, thus it is reasonable to assume that dehydrogenation is complete by 650 K. In that case, the total number of initially adsorbed C₂D₄ molecules per Pt_n cluster can be estimated as the sum of the C₂D₄ desorption plus half the D₂ desorption. This amounts to ~0.3 C₂D₄/Pt atom for both Pt₄ and Pt₈, compared to 0.4 C₂D₄/Pt atom for Pt₇. The numbers of C₂D₄ molecules initially adsorbed per cluster are ~1.1, ~2.7 and ~2.4, respectively, for Pt₄, Pt₇, and Pt₈. Thus, Pt₇ provides significantly more binding sites than the other two cluster sizes on either a per atom or per cluster basis.

Study of small supported clusters is complicated by substrate-mediated adsorption, in which molecules initially land on the alumina support, where they bind too weakly to be stable, diffuse, and bind stably to the Pt_n. For our experiments with 0.1 ML equivalent Pt coverage, the effect is to substantially amplify the effective adsorbate exposure to the clusters, as will be

demonstrated for C_2D_4 below. During the ~20 min elapsing between the start of cluster deposition and the first TPD/R heat ramp, the clusters, on average, are exposed to ~0.04 L of background CO, corresponding to ~0.01 CO impacting per surface atom. During the first TPD/R run, CO desorption amounting to ~0.5 CO molecules/cluster is observed, independent of cluster size. CO binds strongly to Pt_n (see below) and likely competes with C_2D_4 for Pt binding sites. Therefore, we expect that the integrated C_2D_4 numbers are somewhat lower than they would be if no CO were present.

As discussed above, a larger fraction of the Pt atoms is exposed in the surface layer of Pt_7 /alumina compared to that in Pt_8 /alumina, consistent with the observation that more C_2D_4 adsorbs on Pt_7 than on Pt_8 . Clearly; however, understanding the TPD/R experiments requires consideration of how the Pt_n isomer distribution is affected by ethylene adsorption and also of the factors that control branching between ethylene desorption and dehydrogenation.

Before discussing DFT results for ethylene- Pt_n interactions, we consider the question of whether the temperature dependence observed for D_2 desorption is controlled by the energetics of C_2D_4 decomposition or simply reflects the activation energy for desorption of D_2 . This point was tested by studying D_2 TPD, and Figure S2 compares the D_2 desorption from separate samples of Pt_8 /alumina/Ta(110) after 5 L exposure to either D_2 or C_2D_4 at 150 K. It can be seen that for the D_2 exposure, desorption starts at ~160 K compared to ~220 K for the C_2D_4 exposure and is 90% complete by ~400 K, at which point only about half the D_2 from C_2D_4 has desorbed. In this temperature range, D_2 desorption from Pt almost certainly involves recombination of absorbed D atoms; thus, the higher temperatures required to drive D_2 desorption after C_2D_4 exposure suggest that the limiting factor is the activation energy for some step(s) in the C_2D_4 decomposition process rather than the D_2 recombinative desorption energetics.

The desorption spectra were simulated to extract activation energies as described in the Supporting Information, which reports the best-fit energy distributions in Figure S3. Simulation was based on assuming first-order kinetics for the limiting step, as might be expected for intact C_2D_4 desorption. On the basis of this assumption, the desorption energy for C_2D_4 bound on the alumina film is in the ~0.5 eV range, while for C_2D_4 at Pt cluster sites, the desorption energy would range from ~0.6 to 1.4 eV. For D_2 production, under the assumption of a first-order limiting step, the activation energy would be in the 0.7–2.3 eV range. A combination of DFT and coverage-dependent TPD/R studies was used to probe C_2D_4 adsorption and desorption, resulting in a more complex picture of the process.

Because theory on supported cluster systems is computationally demanding due to the large number of isomers and adsorption geometries involved, we focus our DFT work on ethylene adsorption and activation for dehydrogenation as the key processes influencing the kinetics for ethylene and hydrogen desorption. In addition, we chose the Pt_7 /alumina system for the most in-depth work, both experimentally and theoretically. Because the TPD results indicate that roughly three C_2D_4 molecules adsorb initially per Pt_7 , we consider theoretically adsorption of one, two, and three ethylene molecules on the most important Pt_7 isomers and also the factors that influence desorption vs dehydrogenation.

The literature for ethylene binding and hydrogenation/dehydrogenation on various Pt surfaces provides an important insight that aids interpretation of the DFT results. Ethylene

adsorption and decomposition has been extensively studied on various platinum surfaces using techniques such as TPD, reflection/absorption infrared spectroscopy (RAIRS), and high-resolution electron energy loss spectroscopy (HREELS). At temperatures below 100 K, adsorbed ethylene forms di- σ bonds on close-packed $Pt(111)$ ^{15,16} and $Pt(100)$ ¹⁷ surfaces and π -bonds on the stepped sites of $Pt(210)$ and $(1 \times 1)Pt(110)$.¹⁸ On the close-packed surfaces, some of the di- σ bound ethylene desorbs intact at temperatures around 285 K; however, TPD of C_2D_4 and C_2H_4 coadsorbed on $Pt(111)$ also yielded C_2D_3H and C_2H_3D , indicating that recombinative desorption of dissociatively chemisorbed ethylene also contributes to the ethylene desorption signal.¹⁹ At temperatures just above the ethylene desorption peak, H_2 desorption begins, indicating the onset of dehydrogenation. The first dehydrogenation step results in formation of ethylidyne ($\equiv CCH_3$), which has been shown to adsorb in 3-fold hollow sites by HREELS²⁰ and tensor LEED.²¹ Most studies consider ethylidene to be a spectator species.^{22–24} At higher temperatures, the ethylidyne undergoes further decomposition, giving rise to additional H_2 desorption and going to completion by ~700 K. For the stepped surface of $Pt(210)$, some of the π -bound ethylene desorbs at ~250 K, and then the remaining π -bound ethylene dehydrogenates at ~300 K, resulting in desorption of H_2 and formation of adsorbed ethylidyne ($\equiv CCH_2-$, both C atoms bound to the surface), which undergoes further decomposition, giving rise to additional H_2 desorption and going to completion by ~700 K. In contrast, upon heating the $(1 \times 1)Pt(110)$ surface to ~160 K, some of the π -bound ethylene is converted to di- σ bound ethylene. Between 270 and 330 K, the adsorbed ethylene reacts to form carbon atoms and ethylidyne on the surface accompanied by desorption of methane and H_2 . The remaining ethylidyne undergoes complete dehydrogenation by 450 K. Studies on alumina-supported Pt nanoparticles showed that at temperatures below 180 K, ethylene adsorbs in three distinct forms: π -bound ethylene, di- σ bound ethylene, and the ethylidyne species.²⁵ By room temperature, all of the π -bound ethylene desorbs intact, while at higher temperatures, the remaining di- σ bound ethylene is converted to ethylidyne.

From the perspective of interpreting the DFT results, the key insight from these studies is a correlation between the adsorbed configuration of ethylene and its subsequent reactivity.^{22,24,26–29} This correlation, which applies to both Pt surfaces and Pt clusters, is that π -bonded, sp^2 configurations tend to result in hydrogenated products, while di- σ bonded, sp^3 configurations result in dehydrogenated products. For our system, where no hydrogen is added and hydrogenation is not observed, we interpret this correlation as suggesting that the precursor to dehydrogenation is di- σ bonded ethylene, while π -bonded ethylene should tend to desorb intact. Our bonding analysis of ethylene adsorbed to Pt_7 corresponds well to near-edge X-ray-absorption fine-structure (NEXAFS) studies on $Pt(111)$ with di- σ bound ethylene reflecting a bond-length of ~1.5 Å and π -bound ~1.4 Å.²⁹ Moreover, bond angles of $\approx 120^\circ$ and ≈ 97 – 115° reflect sp^2 and sp^3 hybridization present in adsorbed ethylene, respectively. We therefore will use the geometries calculated for adsorbed ethylene as indicators of the propensity to dehydrogenate.

Figure 3 shows the DFT results for ethylene binding to both the single layer and prismatic Pt_7 isomers that were shown in Figure 1. The most stable structures (i) are shown at the top, and additional local minima are shown below, with energetics and thermal populations summarized in Table 1. Recall that for

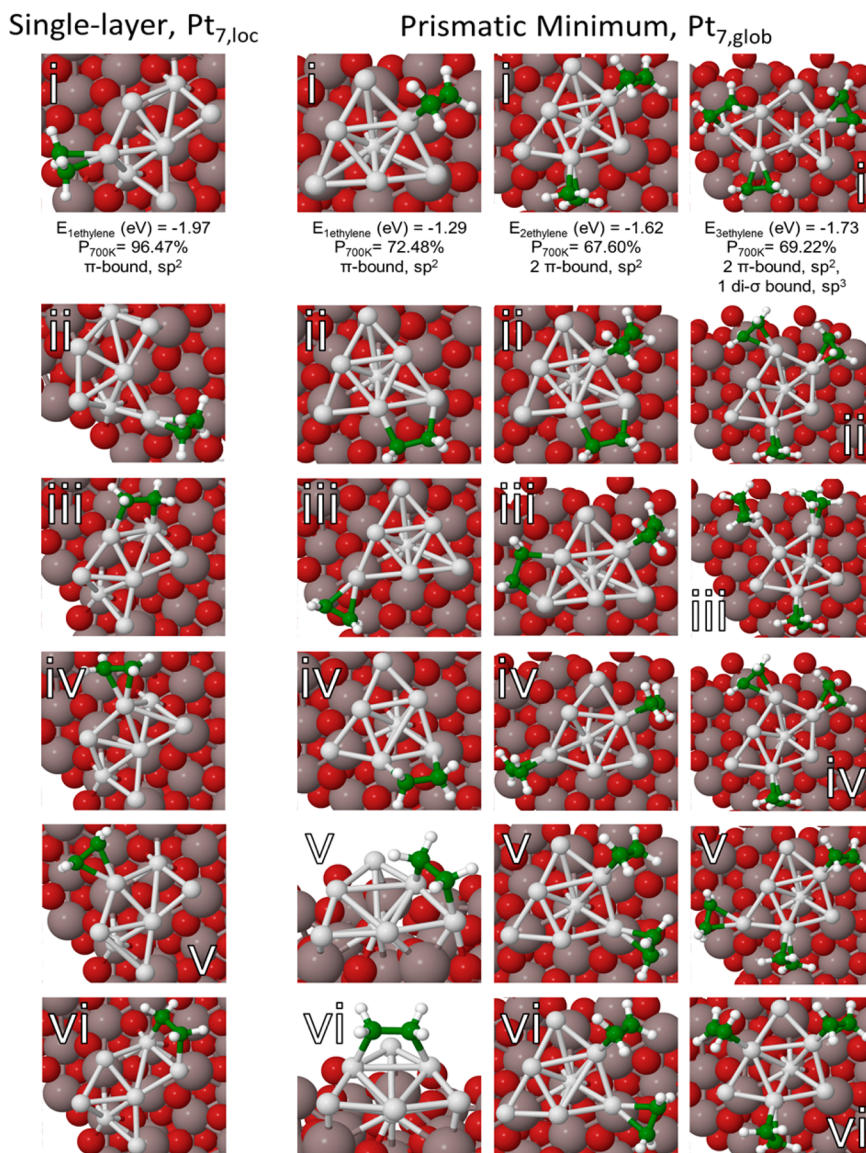


Figure 3. Structures of ethylene binding to Pt_7 . Left column: Binding of a single ethylene molecule to different sites on single-layer Pt_7 . Columns 2–4: Binding of 1, 2, or 3 ethylene molecules in different sites on the global minimum prismatic isomer of Pt_7 . Energetics and bonding analysis are summarized in Table S5, and adsorption geometries and thermal distributions are summarized in Table 2. For additional local minima at each coverage ($n = 2$ or 3), refer to the Supporting Information.

adsorbate-free $\text{Pt}_7/\text{alumina}$, the global minimum is prismatic; however, because the binding energy for the first ethylene molecule is ~ 0.6 eV higher for the single-layer isomer, this becomes the global minimum for $\text{ethylene}_1/\text{Pt}_7$, and a variety of low energy $\text{ethylene}_1/\text{Pt}_7$ geometries based on the single layer isomer are shown in the left column. With one ethylene molecule adsorbed, the prismatic isomers shown in the second column are therefore local minima, stabilized by barriers associated with the considerable rearrangement required to convert to the single layer global minimum.

Bader charge analysis shows that ethylene adsorption is associated with electron transfer from Pt_n to the carbon atoms of ethylene, suggesting that the charges on the adsorbate-free $\text{Pt}_n/\text{alumina}$ isomers should be related to their affinities for ethylene. The charges on each atom given in Figure 1 show that on average, Pt_7 has greater electron transfer from the support compared to that of Pt_8 . Pt_7 isomers take up $1.22\text{--}1.44 \text{ e}^-$ compared to $0.80\text{--}1.24 \text{ e}^-$ for Pt_8 . In addition, the single-layer

Table 1. Boltzmann Populations of Adsorbed Ethylene of $n = 1, 2$, and 3 Coverage in the $\text{di-}\sigma$, sp^3 Configuration (Precursor to Dehydrogenation)

ethylene coverage	$n = 1$	$n = 2$	$n = 3$
$E_n \text{ ethylene,glob (eV)}$	-1.29	-1.62	-1.73
$\Delta Q_{\text{ethylene,glob}} (\text{e})$	0.00	-0.02	-0.30
$\sum P_{450 \text{ K}, \text{sp}^3}$	7.35%	17.51%	84.26%
$\sum P_{700 \text{ K}, \text{sp}^3}$	14.93%	29.42%	69.22%

Pt_7 isomers have higher charge than the prismatic isomers and less uniform charge distributions, with some Pt atoms carrying the majority of the negative charge. Pt_8 , which has only prismatic isomers, has more uniform and lower charge distributions.

In principle, the extent of Pt_n charging can be probed by XPS, and Pt 4d spectra for $\text{Pt}_7/\text{alumina}$ and $\text{Pt}_8/\text{alumina}$ are shown in Figure S4. The stronger Pt 4f peaks were unusable because of Al 2p background. Although the 4d signal is noisy

for 0.1 ML Pt coverage, it appears that the 4d binding energy (BE) for Pt_7 is shifted ~ 0.4 eV to higher energy compared to the Pt_8 BE. We previously reported XPS BEs for Pt_n on glassy carbon³⁰ and indium tin oxide,³¹ and Isomura et al.¹⁰ reported BEs for $\text{Pt}_n/\text{TiO}_2(110)$. In all cases, the Pt_7 BE is higher than that for Pt_8 , opposite to what might be expected if Pt_7 is more negatively charged than Pt_8 . Note; however, that XPS BEs for small clusters are strongly affected by size-dependent final state effects,^{1,32–34} and size-dependent rehybridization of metal orbitals has recently been identified as another factor in BEs for supported Pd_n .^{35,36} As a result, interpreting the BE shift in terms of the initial state charge is not possible.

Upon ethylene binding, the calculated charge on the Pt binding site increases by ≈ 0.2 – 0.7 e, reflecting electron transfer from Pt to ethylene. Therefore, it is not unreasonable to expect that the more negatively charged cluster isomers and binding sites should tend to have higher ethylene binding energies. For example, the single-layer local minimum is 0.22 e⁻ more negatively charged than the prismatic global minimum, and its ethylene adsorption energy is stronger by 0.68 eV. Therefore, both the larger average alumina-to-Pt_n electron transfer for Pt_7 , and the existence of low-lying single-layer local minima that have the highest alumina-to-Pt_n electron transfer, are consistent with the observation (Figure 2) that Pt_7 binds ethylene more strongly than Pt_8 . The fact that Pt_7 also binds more ethylene in saturation is also consistent with the larger fraction of Pt in the cluster surface layer. At low coverage, the prismatic global minimum Pt_7 structure shows more di- σ ethylene binding (configurations ii and iv–vi, Figure 3, Table S5) than the single-layer local minimum (only configuration iii). The di- σ bound ethylene often carries more negative total charge ($\Delta Q_{\text{ethylene}}$) as compared to its π -bound counterpart at all studied coverages (Table 1 and Tables S5–S7).

Because at the ethylene exposure temperature (150 K), the prismatic isomer of Pt_7 should dominate, and because of the great computational expense, coverage-dependent ethylene binding was studied only for starting geometries based on this isomer. All possible adsorption sites (atomic, bridging, and hollow) were evaluated for this global minimum Pt_7 isomer, and the six lowest energy geometries were used in further analysis. The lowest energy minimum for one ethylene adsorbed on prismatic Pt_7 was used as the starting geometry for adding the second ethylene, and the resulting two-ethylene minima were taken as starting geometries for adding the third. This is an approximation because the lowest energy geometry is not necessarily the precursor for higher coverage structures. Thus, there is some uncertainty as to whether the thermal populations in our coverage study include all important structures; however, the results provide at least qualitative insights.

With one or two ethylene molecules adsorbed, the prismatic Pt_7 starting geometry is retained in the optimized structures, but for three adsorbed ethylene molecules, optimization from many of the prismatic starting geometries led to single layer isomers, dominating the thermally accessible ensemble (>78% Boltzmann populations at 450 and 700 K). As noted, even for the first adsorbed ethylene, the single layer structure is lower in energy than the prismatic isomer, but the prismatic isomer is stabilized by a barrier of unknown height. The same is likely true for two ethylene molecules, but clearly, the isomerization barrier vanishes when the third ethylene binds. Therefore, one inference from DFT is that adsorption of ethylene will tend to drive transition toward single layer isomers and that such

structures are therefore likely to be more important in the experiments than would be suggested by consideration of only adsorbate-free Pt_n geometries. Additionally, we observe that as ethylene coverage increases and cluster geometries flatten, the populations of di- σ ethylene binding geometries, which are precursors to dehydrogenation, also increase from 7.35 to 84.26% at 450 K, i.e., at the peak of D_2 desorption (Table 1).

A coverage-dependent TPD/R experiment was performed on $\text{Pt}_7/\text{Al}_2\text{O}_3$ to gain further insight into the energetics and dynamics of ethylene desorption and the competition between desorption and dehydrogenation. Figure 4 compares C_2D_4 and

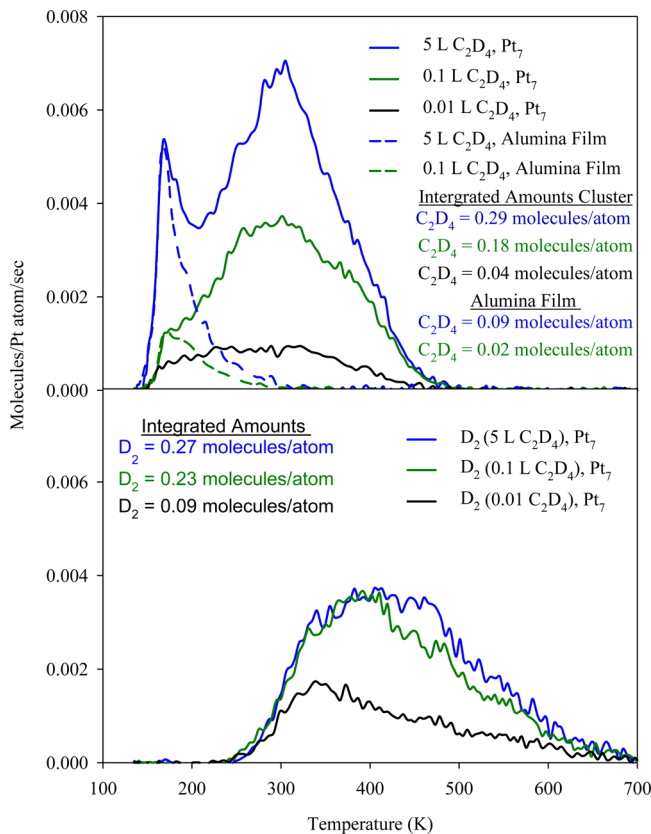


Figure 4. Desorption of unreacted C_2D_4 (top frame) and D_2 products (bottom frame) during TPR after 150 K C_2D_4 exposure to $\text{Pt}_7/\text{alumina}$ and the cluster-free alumina support. Desorption of C_2D_4 from the cluster-free alumina support was scaled as if the sample contained an identical Pt loading as the $\text{Pt}_7/\text{alumina}$ samples. Each set of spectra results from individual experiments with either a 5, 0.1, or 0.01 L C_2D_4 exposure. Each frame also includes the total integrated C_2D_4 and D_2 desorption per Pt atom for each experiment.

D_2 desorption from separately prepared $\text{Pt}_7/\text{alumina}$ samples exposed to 5, 0.1, and ~ 0.01 L of C_2D_4 at 150 K, otherwise following the same procedure as in Figure 2. For comparison, C_2D_4 desorption from the cluster-free alumina film is also shown for 5 and 0.1 L C_2D_4 exposures. The figure also gives the numbers of C_2D_4 and D_2 molecules desorbing per Pt atom, calculated by subtracting the desorption from cluster-free alumina and then integrating.

For the $\text{Pt}_7/\text{alumina}$ samples, C_2D_4 desorption clearly is mostly from sites on alumina at the lowest temperatures and from Pt-associated sites at temperatures above ~ 200 K. The Pt-associated desorption feature is quite broad, which normally would be taken as evidence for a wide distribution of

desorption energies, as suggested by the fits to the TPD/R results discussed above. In that scenario, we would expect desorption to shift to higher temperatures for decreasing coverage, because in subsaturation coverages, adsorbates should tend to diffuse to and desorb from the most stable sites available. Furthermore, if C_2D_4 in the strongest di- σ binding sites has the highest probability of decomposing rather than desorbing intact, we might expect that the branching to D_2 should increase with decreasing coverage, as is observed from ~32% in the 5 L exposure to ~52% for the 0.01 L exposure.

The coverage dependence of the desorption temperatures do not fit this simple scenario, however. The C_2D_4 desorption spectrum is weakly coverage dependent, and if anything, there is less desorption at the highest temperatures for the lowest coverage. Furthermore, while the upper and lower temperature limits for D_2 desorption are independent of initial coverage, the peak of D_2 production shifts to substantially lower temperatures for lower initial C_2D_4 coverage. Given the DFT results showing that the relative stability of different Pt_7 isomers is dependent on C_2D_4 coverage and that the isomer distribution evolves with temperature, we believe that the measured desorption temperature distributions reflect complex dynamics involving changes in cluster structure as part of the C_2D_4 desorption and decomposition mechanism.

Figure 4 also illustrates the importance of substrate-mediated adsorption for highly dispersed clusters. Exposure of 5 L corresponds to $1.8 \times 10^{15} C_2D_4$ collisions/cm² or ~1.2 collisions/surface atom. If adsorption at Pt sites occurred only in C_2D_4 collisions on Pt_7 , reducing the C_2D_4 exposure substantially should substantially reduce the C_2D_4 coverage on Pt_7 . Assuming that adsorbed C_2D_4 either desorbs intact or generates two D_2 molecules, and subtracting the contribution from the alumina sites, the initial C_2D_4 coverage on Pt_7 in the 5 L dose is ~2.7 per Pt_7 cluster. For a dose 50 times lower, the coverage is ~2.1 C_2D_4/Pt_7 , and for exposure 500 times lower, the initial coverage is still ~0.6 molecules/ Pt_7 .

Routes of Deactivation. From the perspective of the catalytic properties of small Pt_n /alumina, it is important to understand how the clusters are modified by heating, adsorption, desorption, and dehydrogenation of ethylene. The DFT results suggest that isomerization is likely during the TPD/R cycle, and the second TPD/R runs on each sample (**Figure 2**) indicate that irreversible changes also occur. The amount of C_2D_4 desorbing at high temperatures decreased in the second run with an offsetting increase in desorption at low temperatures. The total amount of C_2D_4 desorbing in the second run was ~0.3 molecules per Pt atom for all three samples, which is essentially identical to the amount observed in the first runs for Pt_4 and Pt_8 . For Pt_7 , however, ~0.3 C_2D_4/Pt atom represents a ~25% drop compared to the first run. As shown above, C_2D_4 adsorbed on the alumina support all desorbs intact at low temperatures, and the results in the first and second TPD/R runs are identical for cluster-free alumina. For Pt_n /alumina, it is reasonable to assume that the alumina contribution to the C_2D_4 signal is also identical in the first and second runs, thus implying that C_2D_4 desorption from Pt sites shifted to lower temperatures in the second TPD/R run, i.e., the ethylene-Pt desorption energies substantially decreased. The temperature dependence for D_2 desorption did not differ dramatically between the first and second TPD/R runs; however, the integrated amount of D_2 dropped by ~60–70%. This behavior is what would be expected if the activation energy for C_2D_4 dehydrogenation is unchanged in the second

run so that more of the C_2D_4 , which is bound more weakly in the second run, desorbs at temperatures below the onset for decomposition.

In the second TPD/R run, the dependence on deposited cluster size is much weaker than that in the first, where Pt_7 stands out. This change could indicate that thermal or adsorbate-induced ripening or sintering generates a size distribution that no longer depends on the deposited size; however, there are other possibilities. DFT suggests that the larger amount, stronger binding, and greater propensity toward dehydrogenation of C_2D_4 on Pt_7 compared to that on Pt_8 (based on its structural and electronic characteristics) is related to the existence of a larger number of strong di- σ binding sites on Pt_7 . If carbon left on the surface by D_2 desorption in the first TPD/R run tends to poison the strong di- σ binding sites, this would reduce both the average C_2D_4 binding energy in the second TPD/R run, and the amount of D_2 produced, in line with observations. The fact that more D_2 is produced per Pt atom in the first TPD/R run for Pt_7 than either Pt_4 or Pt_8 implies additional carbon poisoning for Pt_7 in the second run, tending to bring its binding/reactivity properties more in line with those of Pt_4 and Pt_8 .

Several experiments were done to provide additional insight into how TPD/R changes the clusters. CO binds strongly to Pt and weakly to alumina, providing an alternative probe of the effect of different experimental manipulations on the availability of Pt binding sites. **Figure 5** compares CO TPD for a set of Pt_7 /

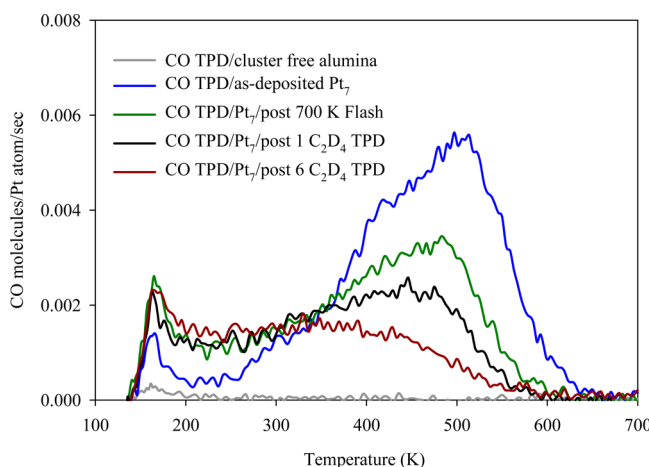


Figure 5. CO desorption from a Pt_7 /alumina compared with CO desorption from separately prepared Pt_7 /alumina samples after a 700 K flash, a single C_2D_4 TPD, and 6 consecutive TPD's. All samples were exposed to 10 L of CO at 150 K.

alumina/Ta(110) samples that were each first exposed to a particular manipulation and then probed by CO TPD (10 L ^{13}CO exposure at 150 K, heating at 3 K/sec to 700 K). Little CO desorbs from the alumina support, but for as-deposited Pt_7 /alumina, strong bimodal CO desorption is observed with a low temperature component peaking at ~165 K and a broader high temperature component peaking at ~520 K. Simply heating Pt_7 /alumina to 700 K in vacuum results in a ~40% decrease in high temperature CO desorption and an increase in low temperature desorption. We previously studied CO TPD from Pt_n /alumina/Re(0001) ($2 \leq n \leq 18$)⁹ with similar results to the Pt_7 /alumina/Ta(110) TPD shown here. We found that the high temperature CO desorption intensity during the first TPD on Pt_n /alumina/Re(0001) increased substantially with

increasing cluster size. Therefore, we can conclude that the decrease in high temperature CO desorption following 700 K heating in **Figure 5** cannot be explained by thermal sintering or ripening alone. We are not claiming that sintering/ripening are unimportant, but there must be other changes as well. For example, 700 K annealing may cause changes in the as-deposited isomer distribution.

After a single C_2D_4 TPD/R run, there is a 55% decrease in the high temperature CO desorption, and the decrease is ~75% for CO TPD following 6 C_2D_4 TPD/R runs. Both heating and C_2D_4 TPD/R result in an increase in low temperature CO desorption, but overall, the total amount of CO desorbing decreased by ~25% after 700 K heating and ~40 and 50%, respectively, for 1 and 6 ethylene TPD/R runs. The larger effect of C_2D_4 TPD/R compared to that of 700 K heating is attributed to carbon left on the surface by D_2 desorption, blocking the Pt binding sites associated with high temperature CO desorption.

To provide additional insight into how ethylene binds to Pt_n /alumina and the effects of heating and carbon deposition, we did two types of He^+ ISS experiments. **Figure 6** compares raw

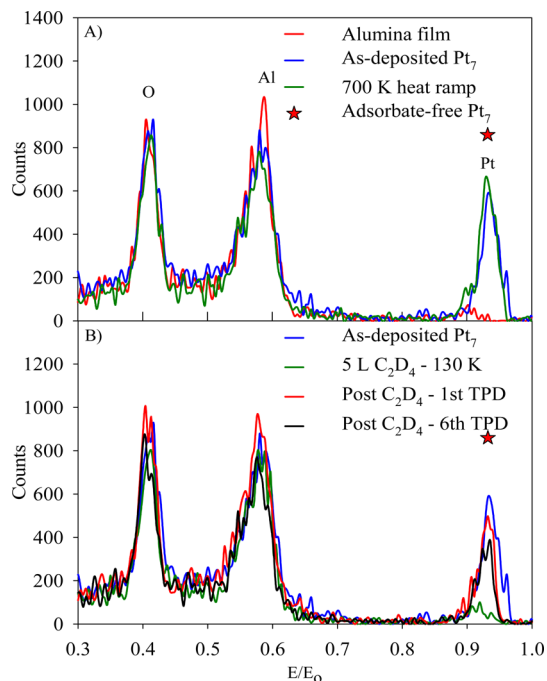


Figure 6. Raw ISS spectra for Pt_7 /alumina samples (a) after a 700 K flash and measured as-deposited. Extrapolated as-deposited is represented by the star. (b) Raw ISS spectra Pt_7 /alumina sample after the sample was exposed to 5 L of C_2D_4 at a 150 K and cooled to 130 K, after one C_2D_4 TPD, and after six consecutive C_2D_4 TPDs.

ISS data for Pt_7 /alumina after a variety of experimental operations. The peaks primarily result from scattering of He^+ from single Pt, O, and Al atoms in the top layer of the sample. He^+ signal from multiple or subsurface scattering events is strongly attenuated, contributing mostly to the weak background at $E/E_0 \leq 0.6$.^{37,38} Small Pt clusters, where most or all of the Pt atoms are in the surface layer, should give large Pt ISS signals and also cause some attenuation of ISS signals from the alumina support, although the attenuation should be small because the Pt_n coverage is low. Isomerization or agglomeration of clusters to form multilayer structures reduces the fraction of

Pt in the surface layer, which should appear as a drop in Pt ISS signal. Similarly, adsorbates binding on top of the clusters attenuate the Pt ISS signal, while adsorbates binding on the alumina or around the cluster periphery have little effect on Pt signal but may attenuate signal from alumina.

In the top frame of **Figure 6**, ISS data are compared for the cluster-free alumina film, as-deposited Pt_7 /alumina, and Pt_7 /alumina that was heated to 700 K in ultrahigh vacuum (UHV). Note the presence of a small peak at $E/E_0 \approx 0.9$ for cluster-free alumina, attributed to a ~1% concentration of Ta in the surface layer from diffusion during high temperature alumina growth on the Ta(110) substrate.^{39,40} For samples with Pt_n deposited, this Ta signal is presumably still present, underlying the much stronger Pt peak. Because the Ta intensity is so small, we have not attempted to subtract it.

When as-deposited Pt_7 /alumina is heated to 700 K, there is a small increase in Pt ISS intensity. As discussed above, TPD shows that the as-deposited clusters are decorated with ~0.5 adventitious CO molecules per cluster, and **Figure S6** implies that these CO molecules bind such that they attenuate ISS signal from the Pt clusters. Using the extrapolation procedure illustrated in **Figure S5** and detailed previously,^{9,41,42} we estimate the attenuation to be ~30%, and the star in **Figure 6** indicates the estimated value for adsorbate-free Pt_7 /alumina. CO desorbs by 700 K (**Figure 5**), which should restore the Pt ISS intensity; thus, the fact that only a small signal increase occurs implies that heating also drives morphology changes that offset the expected increase. From the size of the offset, we can rule out formation of large three-dimensional particles, but thermal isomerization from single layer to prismatic isomers or modest ripening of the cluster size distribution are possible.

The lower frame of **Figure 6** compares the effects of C_2D_4 exposure and TPD/R. One sample was exposed to 5 L of C_2D_4 at 150 K and then probed by ISS while cold, resulting in Pt ISS attenuation by ~90% compared to the adsorbate-free limit, demonstrating that C_2D_4 adsorbs in geometries that strongly attenuate He^+ signal from Pt. The Al and O ISS signals are attenuated by much smaller amounts, consistent with the TPD data, indicating that little C_2D_4 adsorbs on alumina at this temperature. ISS data are also shown for a Pt_7 /alumina sample after a single C_2D_4 TPD/R run under the conditions of **Figure 2** and for another sample run through 6 consecutive TPD/R runs prior to ISS analysis. After one TPD/R run, the Al and O intensities recover to the pre-exposure values, but the Pt ISS intensity remains ~15% below the as-deposited value or ~45% below the adsorbate-free limit. This post TPD/R value is ~25% smaller than that measured after 700 K heating, and this additional attenuation is not surprising given that we know that carbon is left on the surface by D_2 desorption (~1.4 C atoms/ Pt_7). **Figure S7** gives the integrated D_2 desorption signal during 6 sequential C_2D_4 TPD/R runs, allowing us to estimate that a total of ~3.4 C atoms are left behind per initially deposited Pt_7 . If this carbon remains on top of Pt, it would cause at least a substantial fraction of the ~65% Pt ISS attenuation observed after 6 TPD/R runs, but the attenuation may also reflects sintering or other changes in the Pt morphology. We also probed the residual carbon by XPS. No C 1s signal was detected after one or two TPD/R runs, but as shown in **Figure S8**, after six runs, C 1s signal was observed, albeit too weak for accurate quantitation.

Temperature-dependent ISS (TD-ISS) provides more detailed information about the nature of the adsorbate binding on Pt_7 . TD-ISS is essentially a C_2D_4 thermal desorption experi-

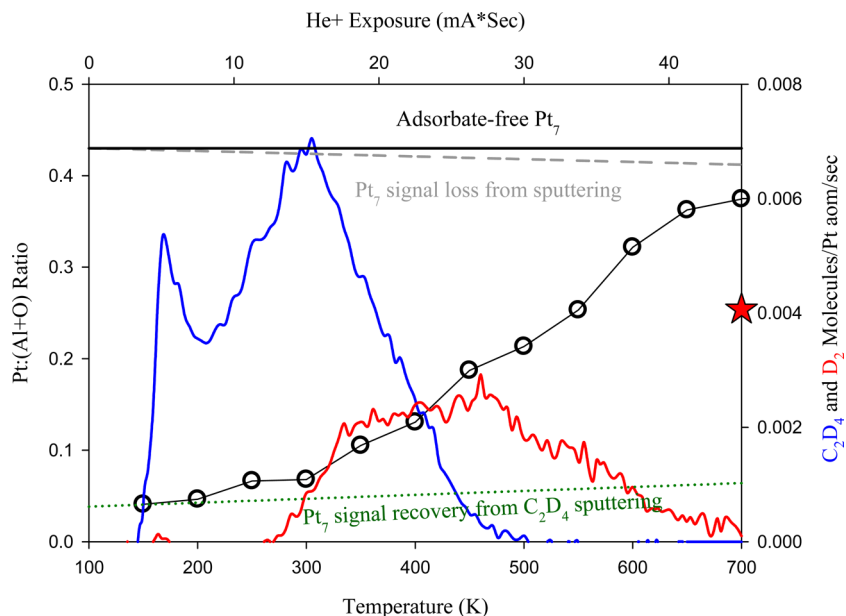


Figure 7. Pt/(Al + O) ISS intensity ratios for Pt₇/alumina after exposure to 5 L of C₂D₄ at 150 K and during a sequence where the sample was heated to the indicated temperatures (black circles). The as-deposited Pt intensity and calibrated rates of Pt recovery from C₂D₄ sputtering and for loss of Pt signal due to sputtering are represented by dashed lines. The Pt/(Al + O) intensity ratio (red star) was measured after completion of a single ethylene TPD cycle.

ment in which a Pt₇/alumina sample was dosed with 5 L of C₂D₄ at 150 K and then characterized by ISS. The sample temperature was then increased in 50 K steps, with ISS measurements at each step. Figure 7 plots the Pt ISS intensities, normalized to the sum of Al and O intensities, as a function of temperature (open circles). The top axis gives the cumulative He⁺ exposure to the sample at the time the Pt ISS peak was being measured at each temperature. For comparison, the C₂D₄ and D₂ desorption data from Figure 2 are superimposed, and a horizontal solid line indicates the expected intensity for adsorbate-free Pt₇, estimated as shown in Figure S6. Comparing the first point at 150 K to the value for adsorbate-free Pt₇/alumina, we see that 5 L C₂D₄ exposure at 150 K resulted in attenuation by ~93%, essentially the same attenuation seen in the raw ISS data in Figure 6. From TPD, we know that this initial exposure leads to adsorption of ~2.7 C₂D₄ molecules associated with the clusters with some additional C₂D₄ bound on the alumina. The expectation is that as the sample is heated and C₂D₄ desorbs or decomposes, the Pt ISS signal should recover.

To interpret the results quantitatively, it is necessary to understand how He⁺ sputtering of Pt and C₂D₄ affects the Pt ISS signal. The extrapolation experiment (Figure S5) also gives the decay rate of Pt ISS signal as a function of He⁺ exposure, and this is plotted in Figure 6 as a gray dashed line labeled “Pt signal loss from sputtering”. For C₂D₄-covered Pt₇/alumina, He⁺ sputter removal of C₂D₄ will tend to increase the Pt signal, and this rate was measured in an experiment where a sample was dosed with 5 L of C₂D₄ at 150 K and then repeatedly probed by ISS while held at 150 K (green dotted line labeled “Pt signal recovery by sputtering”). The Pt ISS intensity just after a single TPD/R cycle (Figure 7) is indicated on the right axis by a red star.

As shown by the superimposed TPD/R data, by 200 K, the lowest temperature C₂D₄ component has desorbed, but there is no recovery of Pt ISS signal beyond that expected from C₂D₄ sputtering. By 400 K, most of the C₂D₄ desorption and ~30%

of D₂ desorption should have occurred, i.e., 85% of the initial C₂D₄ should have either desorbed or decomposed, but the Pt signal recovered to only ~30% of the adsorbate-free value. By 550 K, ~95% of the total amount of C₂D₄ and D₂ desorption should have occurred, but the Pt ISS signal was still ~35% below that expected for adsorbate-free Pt₇/alumina. Note that the intensity at this point is essentially identical to that observed immediately after a TPD/R experiment (red star). The Pt ISS intensity continued to increase and then leveled off above ~600 K at a value well above that seen after a TPD/R run (red star) but ~10% below the value that would be expected based on the “Pt signal loss from sputtering” trend line.

We interpret the results as follows. The TPD component below 200 K is associated with C₂D₄ bound on alumina (Figure 2); thus, its desorption is not expected to have any effect on the Pt ISS signal, as observed. By 300 K, ~50% of the initial C₂D₄ has desorbed, including a significant fraction of the Pt-associated C₂D₄, but there is only modest recovery of Pt signal, indicating the weakly bound C₂D₄ is in sites where it does not strongly attenuate Pt ISS signal. Only as the more strongly bound C₂D₄ desorbs or decomposes at higher temperatures does the Pt signal recovery accelerate, indicating that this strongest C₂D₄ binding component is in sites that are efficient at attenuating ISS from Pt₇. TPD/R shows that it is this strongly bound C₂D₄ that is most likely to decompose, generating D₂. Given our 45° angle of incidence and detection along the surface normal, we expect that these sites should be generally on top of the clusters. The fact that Pt ISS recovery reaches only 90% of the adsorbate-free limit is not surprising because we know that carbon is left on the surface by D₂ desorption. Indeed, the substantially lower Pt ISS signal measured after a TPD/R run (red star) suggests that without the effect of He⁺ sputtering throughout the TD-ISS run, even more decomposition products are left on the cluster surface.

During an earlier study of CO interactions with Pt_n/alumina/Re(0001), we measured but did not publish a TD-ISS study of

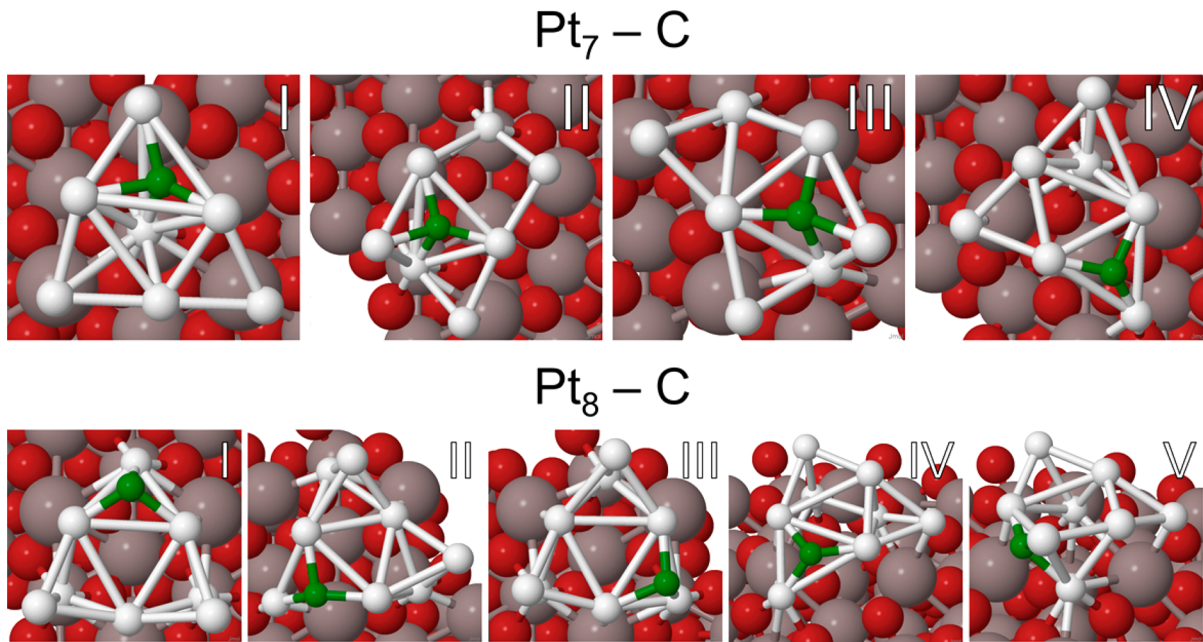


Figure 8. First-order approximation of coking on Pt_7 and Pt_8 : lowest-energy structures for a single C atom adsorbed on these clusters.

CO binding for $\text{Pt}_4/\text{alumina}/\text{Re}(0001)$, and this data is shown in Figure S6 for comparison. The aspect that is relevant to the C_2D_4 results here is that the experiment shows that for CO, the strongest binding sites are also those which cause the largest Pt ISS attenuation, i.e., sites on top of the Pt clusters. A similar conclusion was reached in TD-ISS studies of CO on Pd_n/TiO_2 ⁴¹ and $\text{Pd}_n/\text{alumina}$.

Finally, DFT was also used to examine carbon atom binding to Pt_7 and Pt_8 to determine the most stable binding geometries and also to see if the propensity for coking has a role in the observed efficiency of dehydrogenation on these clusters. Shaikhutdinov et al. noted that in alumina-supported Pd catalysts, carbon deposits began to form at ca. 550 K from di- σ bound ethylene.²⁴ As a first approach to understanding coking, we analyzed C-sticking energetics for isomers of deposited Pt clusters whose Boltzmann populations sum to >99% at 700 K. By summing the C-sticking energies for the Boltzmann-weighted populations for Pt_7 and Pt_8 (i.e., $\sum P E_C$), we obtain an estimate of the coking susceptibility of the isomer ensemble for each cluster size. Higher affinity to C should also correlate with a lower barrier to the dehydrogenation vs desorption.

Pure Pt clusters succumb to coking at higher temperatures due to the increasing population of isomers with very little resistance to carbon deposits (Figure 8). For Pt_7 , $\sum P E_C$ decreases with increasing temperature from -7.30 eV at 450 K to -7.38 eV at 700 K. For Pt_8 , $\sum P E_C$ remains high at > -8.0 eV (see Table 2 for details). This suggests that Pt_8 should undergo coking more readily. The electrophilic C pulls electrons from the Pt clusters, resulting in a ΔQ_C of -0.40 to -0.56 eV (Figures S14 and S15). C preferentially adsorbs on a hollow site with 3–4 Pt–C bonds and prefers the more electron-rich isomers of Pt_7 (Figure 1, isomers II–IV) and Pt_8 (Figure 1, isomers I–IV). We note that catalyst deactivation is a complicated process that may involve the buildup of the C-rich deposits, cluster ripening, and more dramatic restructuring, and it is not fully captured by theory. Experimentally, it is clear that Pt_7 deactivates more strongly after the first TPD run.

Table 2. Adsorbed Isomers with C

cluster	isomer	E_C (eV)	$\sum P_{450\text{K}} E_C$ (eV)	$\sum P_{700\text{K}} E_C$ (eV)
$\text{Pt}_7\text{-C}$	I	-7.05	-7.30	-7.38
	II	-8.03		
	III	-7.70		
	IV	-7.61		
$\text{Pt}_8\text{-C}$	I	-8.17	-8.16	-8.12
	II	-7.60		
	III	-8.36		
	IV	-7.90		
	V	-7.27		

CONCLUSIONS

We reported on ethylene dehydrogenation on size-selected, alumina-deposited subnano Pt clusters accessed via a combination of experiment and theory. Remarkably, deposited Pt_7 is found to be significantly more active than deposited Pt_8 and Pt_4 , which in turn have comparable activities. Pt_7 also deactivates more easily through a number of potential ways, including coking and ripening. Throughout this study, we found that understanding many aspects of the experimental results requires consideration of the accessible ensemble of cluster isomers and how this evolves with C_2D_4 coverage and temperature. For example, the higher C_2D_4 binding affinity and dehydrogenation branching for Pt_7 compared to those of Pt_8 can be recovered only if multiple cluster minima are considered. Furthermore, the importance of single-layer geometries becomes obvious only after realistic coverage is included because C_2D_4 binding drives a transition to single layer isomers where binding is stronger and more likely to result in dehydrogenation. From the dependence of ethylene activation by more negatively charged Pt atoms, it can be proposed that surfaces that charge Pt cluster more should be better supports for Pt catalysts for dehydrogenation. In addition, pronounced differential affinity for C binding is seen only in the ensemble. These results call for a change in paradigm when subnano cluster catalysts are characterized computationally, tracking

isomer distributions with and without the adsorbate(s) of interest.

METHODOLOGY

Experimental Section. The experiments were performed using a cluster deposition/surface analysis instrument described previously,^{41,43} which allows *in situ* sample preparation and characterization. Briefly, the instrument consists of a laser vaporization cluster ion source that feeds into a mass-selecting ion deposition beamline that terminates in a UHV chamber (base pressure $\sim 1.5 \times 10^{-10}$ Torr). The main UHV chamber is equipped for sample cleaning and annealing and houses a differentially pumped mass spectrometer for TPD/TPR studies and hardware for sample characterization by XPS and low energy ISS.

The model catalyst supports were prepared alumina films grown on a 7×7 mm Ta(110) single crystal (Princeton Scientific Corporation), which was spot-welded to tantalum heating wires that were attached to a liquid-nitrogen cooled cryostat mounted at the end of a manipulator. The sample could be cooled to ~ 120 K and resistively heated to ~ 1200 K. A filament mounted directly behind the sample that allowed heating by electron bombardment to temperatures greater than 2100 K. Sample temperature was monitored by a type C thermocouple spot-welded to the back side of the crystal. Because type C thermocouples have low output at temperatures below 300 K, the temperature scale was calibrated by temporarily attaching an additional type K thermocouple, with the result that the two thermocouples agreed to within 3 K over the 120–1000 K range where type K can be used.

Alumina thin films were grown using procedures adapted from work of the Goodman^{44–46} and Madey^{47,48} groups. Aluminum was evaporated from a crucible mounted normal to the Ta(110) surface in 5×10^{-6} Torr $^{16}\text{O}_2$ background pressure while holding the sample temperature at 970 K. Film thicknesses were determined for each sample from the Al 2s and Ta 4d XPS intensities, and for these studies, the growth rate was maintained at ~ 2 Å/min. As discussed by Chen and Goodman, thin (~ 1.5 nm) alumina films grown on Ta(110) show slightly distorted hexagonal symmetry attributed to either the (0001) or (111) face of α -alumina.⁴⁹ We studied the effects of alumina thickness on the core and valence electronic properties of alumina grown on both Ta(110)³⁹ and Re(0001)⁴⁰ and on the CO oxidation activity of Pt_n clusters supported on alumina/Ta and alumina/Re. Because we found that properties became thickness-independent only above ~ 3 nm, we used 3–6 nm thick films in the present study. Note that all experiments were carried out on freshly prepared samples to avoid issues of sample contamination or damage.

Model catalyst preparation began by cooling the cryostat and sample holder until the surface temperature reached 130 K and then flashing it to ~ 2100 K for 5 min to remove any contaminants (including the previous alumina film) and annealing the crystal. XPS and ISS of the surface after this heat treatment showed no contamination with the exception of submonolayer amounts of surface oxygen. The sample was then lowered into a small UHV-compatible antechamber, where it was isolated from the main chamber by a triple differentially pumped seal to the cryostat. The antechamber was then flooded with 5×10^{-6} Torr of O₂, and the alumina film was grown.

Following XPS characterization of the alumina film, the sample was flashed from ~ 120 to 800 K to desorb any

adventitious adsorbates that might have adsorbed during XPS. To minimize exposure of the deposited clusters to background gases, deposition of mass-selected Pt_n ($n = 4, 7$, or 8) clusters was done as the sample cooled back to 120 K, beginning when the sample reached 300 K. During deposition, the sample was positioned directly behind a 2 mm in diameter exposure mask, which defined the size of the cluster spot on surface. The Pt_n coverage was monitored via the neutralization current of the soft landed (~ 1 eV/atom) clusters on the support, and deposition was terminated for all samples such that they all had identical Pt loading of 1.5×10^{14} atoms/cm² (~ 0.1 ML), differing only in the size of clusters deposited. Deposition took 5–15 min.

For TPD/R measurements, a differentially pumped mass spectrometer (UTI 100 C with Extrel electronics) was used, viewing the main chamber through the ~ 2.5 mm diameter aperture in the tip of a skimmer cone. The skimmer cone is surrounded by four 6 mm diameter dosing tubes that point at the sample position and can be connected to either continuous or pulsed valves. For dosing, the sample was positioned with the cluster spot centered on the skimmer aperture with a 2 mm separation to allow line of site from the dosing tubes to the cluster area. Calibration experiments show that the gas exposure to the cluster spot is ten times greater than the exposure to the chamber walls. For ethylene TPD/R experiments, the samples were exposed to 5 L of C₂D₄ at 150 K sample temperature, chosen to minimize adsorption on the alumina support. The sample was then moved to 0.5 mm distance from the skimmer aperture, cooled to 135 K, and then ramped to 700 K at 3 K/sec while monitoring masses of interest desorbing from the surface. To examine the effects of heating and adsorbate exposure on the clusters, the TPD/R experiment (with fresh ethylene exposure) was repeated multiple times on each sample. Select experiments were done under identical conditions but with C₂D₄ exposures of 0.1 and 0.01 L.

Because CO binds strongly to Pt_n but not to alumina, we also did ¹³CO TPD experiments to investigate the effects of heating and ethylene decomposition on the availability of Pt binding sites. These experiments were carried out by exposing samples to 10 L of ¹³C¹⁶O at 150 K and then ramping the temperature from 135 to 700 K at 3 K/sec while monitoring desorption of ¹³CO and other masses of interest. Because of substrate-mediated adsorption,³⁸ highly dispersed Pt clusters are also efficient at collecting adventitious CO, present in the chamber background at $\sim 5 \times 10^{-11}$ Torr. After correcting the mass 28 TPD signal for C₂D₄ cracking in the ion source, the amount of CO adsorbed onto the clusters was found to be ~ 0.5 CO molecules per cluster for Pt₄, Pt₇, and Pt₈, i.e., approximately half of the clusters have one CO molecule adsorbed, desorbing above 500 K. This adventitious signal is independent of whether the sample was dosed with C₂D₄, i.e., C₂D₄ is not able to displace CO from the clusters. The amount of adventitious CO desorbing from a Pt-free alumina film sample is negligible.

To convert the ion signals measured during TPD/R to absolute numbers of molecules desorbing from the surface, we calibrated the mass spectrometer sensitivity in several ways.^{9,50} Several times during the course of the experiments, we checked the calibration of C₂D₄ and other gases of interest by filling the main UHV chamber with those gases to a measured pressure (correcting for ionization gauge sensitivity) while measuring the resulting ion signals. This results in a well-known flux of molecules effusing through the 2.5 mm diameter skimmer cone

aperture into the mass spectrometer ion source (creating a known number density), allowing us to calculate the calibration factor for each gas. To check for possible changes in electron multiplier gain, this calibration was done daily for argon gas. The accuracy of this calibration approach was checked against calibrations based on desorption of saturated CO layers of known coverage from Pd(111) or Ni(110).⁴¹ We estimate that the calibration should be accurate to $\pm 30\%$, mostly because of uncertainties in the angular distributions for desorption from clusters and the ionization efficiency vs angle.

Low energy ISS was used to observe the effects of cluster size, adsorbate binding, and TPD/R on the fraction of Pt atoms in the surface layer. ISS was done by loosely focusing a beam of 1 keV He⁺ onto the sample at 45° angle of incidence with an energy of 1 keV onto the sample and measuring the energy of He⁺ scattered along the surface normal. Peaks in the resulting energy spectrum are due to scattering of He⁺ from single atoms in the sample surface layer, identifying the masses of those atoms. Multiple scattering or subsurface scattering events contribute to a broad background, which is weak due to low ion survival probability in such trajectories.³⁷ Because ISS is not a nondestructive technique, it was either done on separately prepared samples or on samples at the end of experimental sequences.

Computational. Because the alumina film used in the experiments is structurally similar to α -alumina(0001),⁴⁹ all calculations were done for this surface, and the calculations focused on Pt₇ and Pt₈ because these showed interesting differences in the experiments. Plane wave density functional theory calculations of both gas-phase and adsorbed Pt₇ and Pt₈ were performed using Vienna Ab initio Simulation Package (VASP)^{51–54} with projector augmented wave potentials⁵⁵ and the PBE⁵⁶ functional. Bulk calculations were performed with a 8 × 8 × 3 Monkhorst–Pack k-point grid with large kinetic energy cutoffs of 520.0 eV and a stringent SCF (geometric) convergence criteria of 10⁻⁶ (10⁻⁵) eV, resulting in an optimized lattice constant of $a = 4.807 \text{ \AA}$ and $c = 13.126 \text{ \AA}$ for $\alpha\text{-Al}_2\text{O}_3$ (0001), a slight increase compared to experiment.^{57,58} This overestimation is typical of GGA functionals and corresponds to $<0.1 \text{ \AA}$ increase in lattice constants. The α -alumina slab was modeled as a 3 × 3 unit cell with a vacuum gap of 15 Å and the bottom half of the slab kept fixed. For calculations presented in this paper, large kinetic energy cutoffs of 400.0 eV and convergence criteria of 10⁻⁵ (10⁻⁶) eV for geometric (electronic) relaxations were employed. Only the most thermodynamically stable, Al-terminated surface was explored with an inward relaxation of 89.7% of the surface Al and O layers. Reproducing experimental results of -51 to -63% relaxation would require hydroxylation of the surface and introduce even more permutations of adsorbed cluster configurations.^{59,60} Thus, this is beyond the scope of the current study.

Adsorbed structures were formed from the deposition of the lowest 5–6 gas phase structures under PBE levels of theory *per manum* with a thorough sampling of cluster faces to possible binding sites. Gas phase structures of Pt₈ were found with the Adaptive Force Field Coalescence Kick (AFFCK),⁶¹ an adaptive global minimum and local minima search based on the Coalescence Kick (CK).⁶² For Pt₇, structures from a study by Tian et al. were further optimized under VASP/PBE levels of theory, resulting in a new structure (isomer II in Figure S9 and Tables S1 and S2).⁶³ A CK search also uncovered a new configuration, isomer III (see Figure S9 and Table S2). Note

that the order of clusters composed of seven or more atoms will often be DFT method-dependent.⁶¹ This is further discussed in detail in the Supporting Information, utilizing the TURBO-MOLE V6.6 program with def2-TZVP basis and both pure (hybrid) versions of the functionals, PBE (PBE0) and TPSS (TPSSh), respectively.

The relevant equations regarding formation (E_{form}), adsorption (E_{ads}), and reagent (E_{reag}) energies may be found in the Supporting Information and follow the conventions presented in previous studies.^{64,65} The Supporting Information also includes the relevant equations utilized for statistical and bonding analysis such as the Boltzmann probability for *i*th configuration (P_i) and the Gibbs' entropy (S_G). S_G allows us to estimate at a specific temperature T the entropic contribution (TS_G) to the Helmholtz free energy ($F = U - TS_G$). To evaluate the ensemble effects of local minima at Pt_n, the summation of the Boltzmann-weighted adsorption energies ($\sum P_T E_{\text{ads}} = \sum_i P_{i,T} E_{i,\text{ads}}$) and carbon-sticking energies at a temperature T were calculated ($\sum P_T E_c = \sum_i P_{i,T} E_{i,c}$). For the coverage study of ethylene, the calculated adsorption of ethylene took on the forms:

$$E_{\text{ethylene}} = E_{\text{ethylene}+\text{Pt7ads}} - E_{\text{ethylene,gas}} - E_{\text{Pt7ads}}$$

$$E_{\text{2ethylene}} = E_{\text{2ethylene}+\text{glob,Pt7ads}} - E_{\text{1ethylene}+\text{glob,Pt7ads}} \\ - E_{\text{1ethylene,gas}}$$

$$E_{\text{3ethylene}} = E_{\text{3ethylene}+\text{glob,Pt7ads}} - E_{\text{2ethylene}+\text{glob,Pt7ads}} \\ - E_{\text{1ethylene,gas}}$$

ASSOCIATED CONTENT

Supporting Information

The Supporting Information is available free of charge on the ACS Publications website at DOI: 10.1021/acscatal.7b00409.

Details of computational methods; isomers of gas phase and deposited clusters; clusters with 1–3 adsorbed ethylene molecules; and C with charges, populations, energies, and other properties (Figures S1–S15, Tables S1–S7) (PDF)

AUTHOR INFORMATION

Corresponding Authors

*E-mail: ana@chem.ucla.edu.
*E-mail: anderson@chem.utah.edu.

ORCID

Anastassia N. Alexandrova: 0000-0002-3003-1911
Scott L. Anderson: 0000-0001-9985-8178

Author Contributions

[†]E.T.B. and M.-A.H. equally contributed to this work

Notes

The authors declare no competing financial interest.

ACKNOWLEDGMENTS

This work was supported by the Air Force Office of Scientific Research under a Basic Research Initiative grant (AFOSR FA9550-16-1-0141) to A.N.A. and S.L.A. M.-A.H. acknowledges the UCLA Department of Chemistry and Biochemistry Dissertation Year Fellowship. CPU resources at the DoD High Performance Computing Modernization Program (the United

States Air Force Research Laboratory DoD Supercomputing Resource Center (AFRL DSRC), the United States Army Engineer Research and Development Center (ERDC), and the Navy DoD Supercomputing Resource Center (Navy DSRC) supported by the Department of Defense, XSEDE, and the UCLA-IDRE cluster were used to conduct this work.

■ REFERENCES

- (1) Kaden, W. E.; Wu, T.; Kunkel, W. A.; Anderson, S. L. *Science* **2009**, *326*, 826–829.
- (2) Vajda, S.; Pellin, M. J.; Greeley, J. P.; Marshall, C. L.; Curtiss, L. A.; Ballentine, G. A.; Elam, J. W.; Catillon-Mucherie, S.; Redfern, P. C.; Mahmood, F.; Zapol, P. *Nat. Mater.* **2009**, *8*, 213–216.
- (3) Lee, S.; Molina, L. M.; Lopez, M. J.; Alonso, J. A.; Hammer, B.; Lee, B.; Seifert, S.; Winans, R. E.; Elam, J. W.; Pellin, M. J.; Vajda, S. *Angew. Chem., Int. Ed.* **2009**, *48*, 1467–1471.
- (4) Kwon, G.; Ferguson, G. A.; Heard, C. J.; Tyo, E. C.; Yin, C.; DeBartolo, J.; Seifert, S.; Winans, R. E.; Kropf, A. J.; Greeley, J.; Johnston, R. L.; Curtiss, L. A.; Pellin, M. J.; Vajda, S. *ACS Nano* **2013**, *7*, 5808–5817.
- (5) Campbell, C. T.; Campbell, J.; Dalton, P.; Henn, F.; Rodriguez, J.; Seimanides, S. *J. Phys. Chem.* **1989**, *93*, 806–814.
- (6) Pettiette-Hall, C. L.; Land, D. P.; McIver, R. T., Jr.; Hemminger, J. C. *J. Am. Chem. Soc.* **1991**, *113*, 2755–2756.
- (7) Hansen, T. W.; DeLaRiva, A. T.; Challa, S. R.; Datye, A. K. *Acc. Chem. Res.* **2013**, *46*, 1720–1730.
- (8) Brizuela, G.; Hoffmann, R. *J. Phys. Chem. A* **1998**, *102*, 9618–9624.
- (9) Roberts, F. S.; Kane, M. D.; Baxter, E. T.; Anderson, S. L. *Phys. Chem. Chem. Phys.* **2014**, *16*, 26443–26457.
- (10) Isomura, N.; Wu, X.; Hirata, H.; Watanabe, Y. *J. Vac. Sci. Technol., A* **2010**, *28*, 1141–1144.
- (11) Watanabe, Y.; Wu, X.; Hirata, H.; Isomura, N. *Catal. Sci. Technol.* **2011**, *1*, 1490–1495.
- (12) Zhai, H.; Alexandrova, A. N. *J. Chem. Theory Comput.* **2016**, *12*, 6213–6226.
- (13) Zhai, H.; Alexandrova, A. N. *ACS Catal.* **2017**, *7*, 1905–1911.
- (14) Gao, M.; Lyalin, A.; Takagi, M.; Maeda, S.; Taketsugu, T. *J. Phys. Chem. C* **2015**, *119*, 11120–11130.
- (15) Steininger, H.; Ibach, H.; Lehwald, S. *Surf. Sci.* **1982**, *117*, 685–698.
- (16) Ibach, H.; Lehwald, S. *J. Vac. Sci. Technol.* **1978**, *15*, 407–415.
- (17) Hatzikos, G.; Masel, R. *Surf. Sci.* **1987**, *185*, 479–494.
- (18) Yagasaki, E.; Backman, A. L.; Masel, R. I. *Vacuum* **1990**, *41*, 57–59.
- (19) Janssens, T. V. W.; Zaera, F. *Surf. Sci.* **1995**, *344*, 77–84.
- (20) Kesmodel, L.; Dubois, L.; Somorjai, G. *Chem. Phys. Lett.* **1978**, *56*, 267–271.
- (21) Starke, U.; Barbieri, A.; Materer, N.; Van Hove, M.; Somorjai, G. *Surf. Sci.* **1993**, *286*, 1–14.
- (22) Neurock, M.; van Santen, R. A. *J. Phys. Chem. B* **2000**, *104*, 11127–11145.
- (23) Anderson, A. B.; Choe, S. *J. Phys. Chem.* **1989**, *93*, 6145–6149.
- (24) Shaikhutdinov, S. K.; Frank, M.; Bäumer, M.; Jackson, S. D.; Oldman, R. J.; Hemminger, J. C.; Freund, H.-J. *Catal. Lett.* **2002**, *80*, 115–122.
- (25) Mohsin, S. B.; Trenary, M.; Robota, H. *J. J. Phys. Chem.* **1988**, *92*, 5229–5233.
- (26) Perry, D. A.; Hemminger, J. C. *J. Am. Chem. Soc.* **2000**, *122*, 8079–8080.
- (27) Carlsson, A.; Madix, R. *J. Chem. Phys.* **2001**, *115*, 8074–8082.
- (28) Paz-Borbón, L. O.; Hellman, A.; Thomas, J. M.; Grönbeck, H. *Phys. Chem. Chem. Phys.* **2013**, *15*, 9694–9700.
- (29) Stöhr, J.; Sette, F.; Johnson, A. L. *Phys. Rev. Lett.* **1984**, *53*, 1684.
- (30) Proch, S.; Wirth, M.; White, H. S.; Anderson, S. L. *J. Am. Chem. Soc.* **2013**, *135*, 3073–3086.
- (31) von Weber, A.; Baxter, E. T.; Proch, S.; Kane, M. D.; Rosenfelder, M.; White, H. S.; Anderson, S. L. *Phys. Chem. Chem. Phys.* **2015**, *17*, 17601–17610.
- (32) Chusuei, C. C.; Lai, X.; Luo, K.; Goodman, D. W. *Top. Catal.* **2000**, *14*, 71–83.
- (33) Bagus, P. Chemical information from XPS binding energy shifts: A unified view. *Abstracts of Papers of the American Chemical Society; American Chemical Society: Washington, DC*, March 23–27, 2003; pp U676–U677.
- (34) Dai, Y.; Gorey, T. J.; Anderson, S. L.; Lee, S.; Lee, S.; Seifert, S.; Winans, R. E. *J. Phys. Chem. C* **2017**, *121*, 361–374.
- (35) Kaden, W. E.; Büchner, C.; Lichtenstein, L.; Stuckenholz, S.; Ringleb, F.; Heyde, M.; Sterrer, M.; Freund, H.-J.; Giordano, L.; Pacchioni, G.; Nelin, C. J.; Bagus, P. S. *Phys. Rev. B: Condens. Matter Mater. Phys.* **2014**, *89* (115436), 115431–115438.
- (36) Roberts, F. S.; Anderson, S. L.; Reber, A. C.; Khanna, S. N. *J. Phys. Chem. C* **2015**, *119*, 6033–6046.
- (37) Rabalais, J. W. *Principles and applications of ion scattering spectrometry: surface chemical and structural analysis*; Wiley: New York, 2003; p 336.
- (38) Aizawa, M.; Lee, S.; Anderson, S. L. *Surf. Sci.* **2003**, *542*, 253–275.
- (39) Kane, M. D.; Roberts, F. S.; Anderson, S. L. *Faraday Discuss.* **2013**, *162*, 323–340.
- (40) Kane, M. D.; Roberts, F. S.; Anderson, S. L. *J. Phys. Chem. C* **2015**, *119*, 1359–1375.
- (41) Kaden, W. E.; Kunkel, W. A.; Roberts, F. S.; Kane, M.; Anderson, S. L. *J. Chem. Phys.* **2012**, *136*, 204701–204712.
- (42) Kaden, W. E.; Kunkel, W. A.; Anderson, S. L. *J. Chem. Phys.* **2009**, *131* (114701), 114701–114715.
- (43) Kane, M. D.; Roberts, F. S.; Anderson, S. L. *Int. J. Mass Spectrom.* **2014**, *370*, 1–15.
- (44) Chen, P. J.; Goodman, D. W. *Surf. Sci.* **1994**, *312*, L767–L773.
- (45) Street, S. C.; Goodman, D. W. *Chem. Phys. Solid Surf.* **1997**, *8*, 375–406.
- (46) Lai, X.; Chusuei, C. C.; Luo, K.; Guo, Q.; Goodman, D. W. *Chem. Phys. Lett.* **2000**, *330*, 226–230.
- (47) Wu, Y.; Garfunkel, E.; Madey, T. E. *J. Vac. Sci. Technol., A* **1996**, *14*, 2554–2563.
- (48) Wu, Y.; Garfunkel, E.; Madey, T. E. *Surf. Sci.* **1996**, *365*, 337–352.
- (49) Chen, M. S.; Goodman, D. W. *J. Phys.: Condens. Matter* **2008**, *20*, 264013.
- (50) Kane, M. D.; Roberts, F. S.; Anderson, S. L. *Int. J. Mass Spectrom.* **2014**, *370*, 1–15.
- (51) Kresse, G.; Furthmüller, J. *Comput. Mater. Sci.* **1996**, *6*, 15–50.
- (52) Kresse, G.; Furthmüller, J. *Phys. Rev. B: Condens. Matter Mater. Phys.* **1996**, *54*, 11169.
- (53) Kresse, G.; Hafner, J. *Phys. Rev. B: Condens. Matter Mater. Phys.* **1993**, *47*, 558.
- (54) Kresse, G.; Hafner, J. *Phys. Rev. B: Condens. Matter Mater. Phys.* **1994**, *49*, 14251.
- (55) Kresse, G.; Joubert, D. *Phys. Rev. B: Condens. Matter Mater. Phys.* **1999**, *59*, 1758.
- (56) Perdew, J. P.; Burke, K.; Ernzerhof, M. *Phys. Rev. Lett.* **1996**, *77*, 3865.
- (57) Bourdillon, A.; El-Mashri, S.; Forty, A. *Philos. Mag. A* **1984**, *49*, 341–352.
- (58) Levin, I.; Brandon, D. *J. Am. Ceram. Soc.* **1998**, *81*, 1995–2012.
- (59) Ahn, J.; Rabalais, J. *Surf. Sci.* **1997**, *388*, 121–131.
- (60) Wang, X.-G.; Chaka, A.; Scheffler, M. *Phys. Rev. Lett.* **2000**, *84*, 3650.
- (61) Zhai, H.; Ha, M.-A.; Alexandrova, A. N. *J. Chem. Theory Comput.* **2015**, *11*, 2385–2393.
- (62) Averkiev, B. Geometry and electronic structure of doped clusters via the Coalescence Kick method. Ph.D. Thesis, Utah State University, December 2009.
- (63) Tian, W. Q.; Ge, M.; Sahu, B.; Wang, D.; Yamada, T.; Mashiko, S. *J. Phys. Chem. A* **2004**, *108*, 3806–3812.

(64) Dadras, J.; Jimenez-Izal, E.; Alexandrova, A. N. *ACS Catal.* **2015**, *5*, 5719–5727.

(65) Ha, M.-A.; Dadras, J.; Alexandrova, A. *ACS Catal.* **2014**, *4*, 3570–3580.